JfM PAPERS

Characterization of instability mechanisms on sharp and blunt slender cones at Mach 6

Richard E. Kennedy[1],†, **Joseph S. Jewell**[2], **Pedro Paredes**[3] and **Stuart J. Laurence**[4]

[1]BAE Systems Inc., Durham, NC 27703, USA

[2]School of Aeronautics and Astronautics, Purdue University, West Lafayette, IN 47907, USA

[3]National Institute of Aerospace, Hampton, VA 23666, USA

[4]Department of Aerospace Engineering, University of Maryland, College Park, MD 20742, USA

Experiments are performed to investigate the effect of nose-tip bluntness on the instability mechanisms leading to boundary-layer transition on a 7° half-angle cone in a Mach-6 free stream. The development of disturbances is characterized using a combination of high-speed calibrated schlieren images and pressure measurements, and the data are compared with results computed using the parabolized stability equations. The approximately 414 mm long cone model is equipped with an interchangeable nose tip ranging from sharp to 5.08 mm in radius. For nose tips with a radius $R_N < 2.54$ mm, second-mode instability waves are the dominant mechanism leading to transition. Time-averaged frequency spectra computed from the calibrated schlieren visualizations and pressure measurements are used to compute the second-mode most-amplified frequencies and integrated amplification rates (N factors). Good agreement is observed between the measurements and computations in the linear-growth regime for the sharp-nose configuration at each free-stream condition. Additionally, a bispectral analysis identifies quadratic phase locking of frequency content responsible for the growth of higher harmonics. For nose tips of $R_N \geqslant 2.54$ mm, the schlieren visualization region is upstream of the entropy-layer swallowing length, and second-mode waves are no longer visible within the boundary layer; instead, elongated, steeply inclined features believed to be associated with non-modal instability mechanisms develop between the entropy-layer and boundary-layer edges. Simultaneously acquired surface pressure measurements reveal high-frequency pressure oscillations similar to second-mode instability waves associated with the trailing edge of these non-modal features.

Key words: boundary layer stability, hypersonic flow, transition to turbulence

† Email address for correspondence: rkenn@umd.edu

R.E. Kennedy, J.S. Jewell, P. Paredes and S.J. Laurence

1. Introduction

Laminar-to-turbulent transition of a hypersonic boundary layer can strongly influence surface heating rates and skin friction drag on the surface of a hypersonic vehicle. Understanding and predicting this transition process is essential for efficient hypersonic vehicle design. Significant progress has been made in characterizing the instabilities leading to transition over sharp, slender geometries in recent literature (Marineau *et al.* 2019); however, the introduction of leading-edge bluntness has been shown to change the mechanisms that lead to boundary-layer transition (Stetson 1983) and, at present, these mechanisms are less well understood than their sharp-nose counterparts.

For slender, sharp-nosed, axisymmetric bodies in a hypersonic free stream, it is well established that the dominant mechanism leading to transition is the Mack or second mode (Mack 1975). Second-mode instability waves can be physically interpreted as primarily two-dimensional acoustic waves trapped within the boundary layer. The waves typically have wavelengths on the order of twice the boundary-layer thickness and can exhibit fundamental frequencies from tens of kilohertz to well over a megahertz (Mack 1975). Due to the two-dimensional structure and relatively high frequencies of second-mode disturbances, optical techniques are well suited to their measurement (Parziale 2013; Laurence, Wagner & Hannemann 2014; Casper *et al.* 2016). For example, Laurence, Wagner & Hannemann (2016) performed a series of experiments in the HEG high enthalpy shock tunnel using a 7° half-angle cone with a 2.5 mm radius nose tip in a Mach 6–7.5 free stream, using high-speed schlieren visualizations as their primary measurement technique. Image processing techniques allowed the calculation of propagation speeds and spatial frequency content for second-mode disturbances. Developing upon this methodology, Kennedy *et al.* (2018) applied a calibrated schlieren system in the Arnold Engineering Development Complex (AEDC) Hypervelocity Tunnel 9 using a 7° half-angle sharp-cone model in a Mach-14 free stream. The uniform propagation speed combined with an average temporal spacing between images much smaller than the timescales for development of the wavepackets allowed for the development of a time-signal-reconstruction technique to convert spatial data to temporal data. Using the time-reconstructed signals, these authors were able to calculate second-mode wave frequencies and integrated amplification rates. Significant progress has also been made on quantifying the impact of free-stream conditions on second-mode wave development. Marineau *et al.* (2019) combined pressure measurements from eleven facilities, and compared second-mode wave development for the different free-stream conditions. Maximum second-mode amplitudes grew strongly up to an edge Mach number of approximately 5.8 and varied only weakly thereafter. The initial wave amplitudes, A_0, were found to be inversely proportional to the free-stream unit Reynolds number, Re/m, resulting in higher transition N factors for higher unit-Reynolds-number free streams.

Experimental data describing the instabilities that develop over blunt cones is rather more limited, primarily due to difficulties in generating the free-stream conditions capable of causing laminar-to-turbulent transition on a blunt geometry. Stetson (1983) performed a number of experiments using surface-mounted thermocouples and pressure sensors to measure the mean transition location on a 8° half-angle cone at zero incidence in a Mach-6 free stream. The cone model used an interchangeable nose tip, allowing model configurations with nose-tip radii ranging from nominally sharp to 15 mm. The experimental results showed that, as the nose-tip radius is increased, the onset of transition shifts downstream; however, at sufficiently high nose-tip bluntnesses, this trend reverses and the transition location moves upstream with increasing nose-tip bluntness, a process termed 'transition reversal'. Jewell & Kimmel (2017) analysed the experimental results of

Stetson (1983), using the Stability and Transition Analysis for hypersonic Boundary Layers (STABL) computational fluid dynamics software suite to show that increasing the nose-tip bluntness and entropy-layer swallowing length (X_{SW}) results in a monotonic decrease in the N factors associated with the second-mode instability. Oblique modes were shown to not be responsible for the transition-reversal behaviour. Experimental measurements by Marineau *et al.* (2014) using high-speed pressure transducers and Maslov *et al.* (2006) using hot-wire anemometry showed a similar suppression of second-mode growth for cases where the entropy-layer swallowing length was downstream of the transition onset location.

In light of the failure of the linear stability theory to predict the experimentally observed behaviour for blunt cones, researchers have turned to non-modal stability theory as a potential path for modelling the instability mechanisms. Disturbances undergoing non-modal, or transient, growth can experience locally high amplification while being asymptotically stable. Paredes *et al.* (2019c) computationally investigated these non-modal growth mechanisms, finding that disturbances initiated within the nose tip vicinity undergo non-modal amplification that increased with increasing nose-tip bluntness. These non-modal features were significantly amplified while first-mode, second-mode and entropy-layer modal instability amplification was minimal. Paredes *et al.* (2019b) showed that, unlike second-mode waves that appear as rope-like structures within the boundary layer, planar and oblique waves experiencing non-modal growth exhibit a peak in disturbance magnitude between the entropy-layer and boundary-layer edges. Laser-induced fluorescence-based schlieren images captured of the boundary layer over a $7°$ half-angle cone with a 4.75 mm radius nose tip in a Mach-11.8 free stream by Grossir *et al.* (2014) showed elongated structures with content extending out beyond the boundary-layer edge, in qualitative agreement with the computations of Paredes, Choudhari & Li (2019a); however, their visualization system did not have sufficient temporal resolution to capture individual features as they evolved.

In the present work, high-speed calibrated schlieren visualizations, PCB piezoelectric pressure sensor measurements, and computations performed using both the linear and nonlinear parabolized stability equations (PSE) are used to investigate the transition process on a slender cone using nose tips of various bluntness in a Mach-6 flow. The paper is organized as follows. In § 2 we describe the facility, model and measurement techniques. In § 3 we examine transition on the sharp-nose-cone configuration at different unit Reynolds numbers including both time-averaged results and individual wavepacket development. Measurements for the blunt-nose configuration including simultaneously acquired surface pressure traces and schlieren visualizations of individual instability features are presented in § 4. Concluding remarks are given in § 5.

2. Experimental set-up

2.1. *Facility*

All experiments are carried out in the Air Force Research Laboratory (AFRL) Mach-6 Ludwieg tube, an impulse facility capable of producing two steady-flow test periods, each of approximately 100 ms, per experiment (Kimmel *et al.* 2017). For each experiment presented in the current study, the second steady-flow period is used to acquire measurements. In the current investigation, free-stream unit Reynolds numbers are set between 4.90×10^6 and 22.71×10^6 m^{-1} for individual runs by adjusting the reservoir pressure between 689 kPa and 3.48 MPa. Flow is initiated using a fast-acting valve, and air is used as the test gas. The nozzle throat is 9.42 cm in diameter with an exit diameter of

Experiment	R_N (mm)	M_∞	Re_∞/m ($1/m \times 10^6$)	u_∞ (m s^{-1})	T_∞ (K)	ρ_∞ (g m^{-3})
S1	sharp	6.14	4.90	903	54	18.9
S2	sharp	6.14	7.11	904	54	27.4
S3	sharp	6.14	9.31	903	54	35.8
B1	0.508	6.14	13.7	903	54	52.8
B2	1.524	6.14	18.3	902	54	70.2
B3	2.540	6.14	18.3	902	54	70.2
B4	5.080	6.14	18.3	902	54	70.2
B5	5.080	6.14	22.7	902	54	87.3

Table 1. Tunnel free-stream conditions.
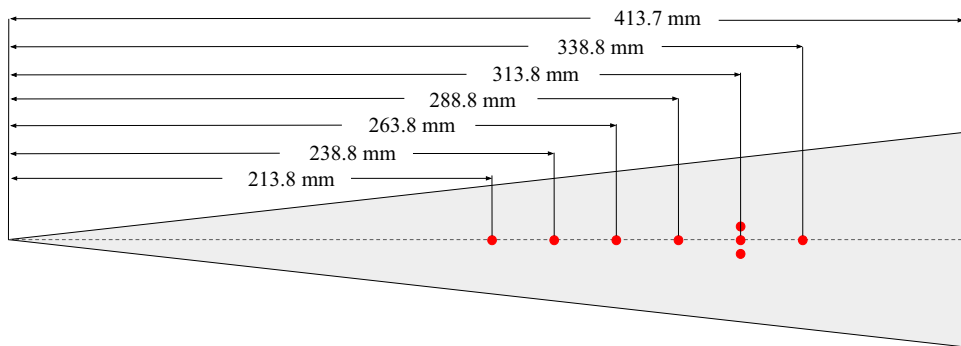
Figure 1. Schematic showing instrumentation layout on cone model with sharp-nose configuration. The red dots indicate the PCB sensor locations.

76.2 cm that terminates in a test chamber approximately 1.27 m in diameter. Optical access is provided by 30.5 cm diameter windows on both sides of the test section. Additional free-stream conditions for each experiment can be found in table 1, and additional information on the facility can be found in Kimmel *et al.* (2017).

2.2. *Model*

The test article is a $7°$ half-angle, slender cone with an interchangeable nose section. With the sharp nose installed, the cone length is 414 mm. Five nose tips of different radii ranging from nominally sharp to 5.08 mm are tested and, for consistency, the surface coordinate s used hereinafter refers to the streamwise distance measured from the tip of the sharp-nose configuration. For all experiments, the model is installed at zero incidence ($\pm 0.5°$) to the free stream. The cone is equipped with eight PCB Piezotronics model 132A and 132B piezoelectric pressure transducers for measuring high-frequency (>11 kHz) pressure fluctuations. Six of the PCB sensors lie along a single streamwise ray as shown in figure 1. The two additional PCB sensors are placed adjacent to the sensor located at $s = 316$ mm and are offset in the circumferential direction by 5.715 mm on either side relative to this plane. The three-sensor-wide array allows for measurements of the spanwise distribution of pressure disturbances. The signals from the PCB sensors are recorded at 5 megahertz. Prior to the start of all experiments, the model is at room temperature, resulting in a wall-to-stagnation temperature ratio of approximately 0.6.

Experiment	R_N (mm)	X_{SW} (m)	M_e	Visualization location s (mm)	Frame rate (f.p.s)
S1	sharp	NA	5.46	257–363	172 131
S2	sharp	NA	5.46	253–367	172 131
S3	sharp	NA	5.46	185–369	234 637
B1	0.508	0.069	3.72	207–358	287 671
B2	1.524	0.330	3.65	275–368	368 421
B3	2.540	0.625	3.41	275–368	368 421
B4	5.080	1.644	2.96	275–368	234 637
B5	5.080	1.769	2.92	275–368	234 637

Table 2. Cone model and camera parameters used for each experiment. The entropy-layer swallowing distance, X_{SW}, and edge Mach number, M_e, are computed as described in §2.4; the latter is calculated at the centre of the visualization region.
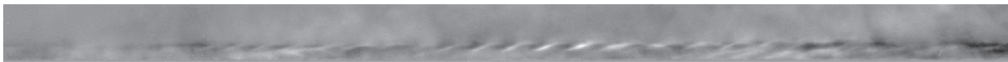
Figure 2. Enhanced schlieren visualization generated by subtracting a mean flow-on image from the image of interest for the sharp nose-tip-radius configuration experiment S1.

2.3. *Schlieren visualizations*

A conventional Z-type (non-focusing) schlieren set-up is utilized to visualize the flow density gradients. Illumination is provided by a Cavilux HF pulsed-diode laser emitting pulses of 30–40 ns duration at 810 nm, released from a 1.5 mm diameter fibre-optic cable. Two 31.8-cm diameter, 1.91-m focal length mirrors are used to collimate the light to pass through the test section and refocus it on the other side. A knife-edge cutoff is used to visualize the density gradients normal to the cone surface, and a Phantom v2512 high-speed camera mounted parallel to the cone surface records the images. For all experiments, the image resolution in the horizontal direction is 1280 pixels, while the number of pixels in the vertical direction is chosen based on the desired camera frame rate and pixel scale. In general, the frame rate is set to be at least one half of the second-mode fundamental frequency predicted by the linear PSE (LPSE), and the number of pixels across the boundary-layer thickness ranges from a minimum of approximately 8 to a maximum of 30. Camera parameters for each experiment are shown in table 2, and an example schlieren image from experiment S1 is shown in figure 2. The slow spatial evolution of the second-mode waves relative to the image acquisition rate allows for the application of the time-signal-reconstruction technique developed in Kennedy *et al.* (2018). For the present experiments, the reconstruction technique is only applied for the cases where the boundary-layer behaviour is dominated by second-mode waves, corresponding to nose-tip radii less than or equal to 1.524 mm. Temporal signals are reconstructed using 3000 images per experiment at 100 streamwise locations evenly spaced across the visualization region.

Calibration of the schlieren system following Hargather & Settles (2012) is performed to enable quantitative measurements. Calibration is required due to the nonlinear schlieren response of the light rays generated by the circular light source. Prior to the start of each experiment, a circular plano-convex lens with a diameter of 25.4 mm and a focal length of 10 m is placed within the schlieren field of view. The incoming collimated light rays are deflected to a degree depending on where they pass through the calibration lens; this in turn causes a pixel-intensity gradient to form across the visualized lens face. The pixel

intensity at any point on the lens face can then be correlated with the known density gradient generated by the calibration lens. For more details associated with the calibration procedure, see Kennedy (2019).

2.4. *Computational method*

Computational analysis is performed using the STABL software suite described by Johnson, Seipp & Candler (1998), Johnson (2000), Johnson & Candler (2005), and implemented in Jewell (2014) and Wagnild *et al.* (2010), as well as the instability analysis solver developed by Paredes (2014) and Paredes *et al.* (2015). First, the mean flow over the cone is computed by the reacting, axisymmetric Navier–Stokes equations with a structured grid, using a version of the NASA data parallel-line relaxation (DPLR) code (Wright, Candler & Bose 1998). This flow solver is based on the finite-volume formulation. The use of an excluded volume equation of state is not necessary for the boundary-layer solver because the static pressure over the cone is sufficiently low (typically, 1–5 kPa) that the gas can be treated as ideal. The mean flow is computed on a single-block, structured grid with dimensions of 361 cells by 359 cells in the streamwise and wall-normal directions, respectively. The inflow gas composition in each case is air with $0.233\,O_2$ and $0.767\,N_2$ mass fractions, and the impact of chemical reactions is negligible as the local maximum temperature does not exceed 550 K for any case.

Grids for each of the five bluntness configurations were generated using STABL's built-in grid generator, and mean-flow solutions were examined to ensure that at least 100 points were placed in the boundary layer for each stagnation pressure. The boundary-layer profiles and edge properties are extracted from the mean-flow solutions during post-processing. The wall-normal span of the grid increases down the length of the cone, from 0.25 mm at the tip to 50 mm at the base, allowing for the shock to be fully contained within the grid for all cases tested. The grid is clustered at the wall as well as at the nose in order to capture the gradients in these locations. The Δy^+ value for the grid, extracted from the DPLR solution for each case, is everywhere less than 1, where Δy^+ is a measure of local grid quality at the wall in the wall-normal direction. Linear PSE stability analyses are performed using the PSE-Chem solver, which is also part of the STABL software suite. The PSE-Chem (Johnson & Candler 2005) software solves the reacting, two-dimensional, axisymmetric, linear PSEs to predict the amplification of disturbances as they interact with the boundary layer. As the temperatures remain sufficiently low, chemistry and molecular vibration effects are omitted. Following Marineau, Moraru & Daniel (2017), a linear function is used to fit the LPSE maximum N factor versus stability Reynolds number (R) results, and a function of the form $f = g/R^h$, where g and h are constants, is used to fit the LPSE results of most-amplified second-mode frequency versus stability Reynolds number for comparison to the experimental measurements. Estimates of the entropy-layer swallowing length as defined by Rotta (1966) are computed using a procedure based on Stetson (1983) to provide an empirically based estimate of the extent of the entropy-layer influence.

The linear non-modal and nonlinear PSE (NPSE) stability analyses are performed following the methodology described by Paredes *et al.* (2019*b*) and Paredes, Choudhari & Li (2020). The methodology used for the analysis of non-modal disturbance amplification over the blunt cone configuration is performed using the harmonic linearized Navier–Stokes equations (HLNSE) as explained by Paredes *et al.* (2019*c*). A variational formulation is used to determine the optimal inflow disturbance that leads to maximum energy gain at a specified downstream position. The HLNSE are discretized with sixth-order finite-difference schemes along the streamwise and

wall-normal coordinates. The discretized NPSE are integrated along the streamwise coordinate by using second-order backward differentiation. Sixth-order finite-difference schemes are used for discretization of the NPSE along the wall-normal coordinate. The maximum number of Fourier modes is set to 12.

3. Transition over sharp-nose configuration

3.1. *Time-averaged results*

We begin our analysis by considering the three experiments performed with the sharp-nose model configuration, for which the second-mode instability is expected to be the dominant transition mechanism (S1–S3). The mean wavepacket propagation speeds, u_{prop}, are determined using the image correlation methodology described in Laurence *et al.* (2014). The images are first processed by a feature detection algorithm to identify the presence and, if applicable, location of a wavepacket. The images are then bandpass filtered around the second-mode fundamental wavelength and a cross-correlation is applied to image pairs throughout the sequence. The mean wavepacket propagation speeds and 95 % error bounds calculated for each condition using approximately 8000 wavepackets per experiment are $787 \pm 28.2 \text{ ms}^{-1}$, $778 \pm 53.4 \text{ ms}^{-1}$ and $804 \pm 36.4 \text{ ms}^{-1}$ for experiments S1, S2 and S3, respectively. Using the Taylor–MacColl solution to compute the cone surface conditions and assuming that these correspond to the boundary-layer edge conditions, we obtain $u_{prop}/u_e = 0.94$–0.97, roughly in line with the previous measurements of Kimmel & Kendall (1991), Laurence *et al.* (2016) and Kennedy *et al.* (2018). Using the reconstructed time signals described in § 2.3, spectra are computed using Welch's method and used to identify the most-amplified second-mode frequencies and amplitudes for each downstream location and experimental condition. Example spectra computed from time signals reconstructed at three streamwise locations for experiment S3 are observed in figure 3. The amplitude of the content at the fundamental second-mode frequency (approximately 240–290 kHz) is observed to increase with increasing downstream location, while the second-mode frequency decreases due to the increasing boundary-layer thickness. Following Stetson (1983), the dimensionless most-amplified second-mode frequency is defined as

$$F = \frac{2\pi f_{max}}{u_{\infty} Re/m}, \tag{3.1}$$

and the stability Reynolds number is defined as

$$R = \sqrt{Re_s}, \tag{3.2}$$

where u_{∞} is the free-stream velocity, Re is the Reynolds number based on the free-stream conditions, f_{max} is the most-amplified second-mode frequency and s is the cone surface coordinate.

In figure 4 we present dimensionless most-amplified second-mode frequencies. In the left plot, measurements are shown for each unit-Reynolds-number condition along with LPSE results, and in the right plot, measurements are shown for experiment S3 along with both LPSE and NPSE results. The NPSE results are computed using an initial disturbance with a finite streamwise velocity at a frequency equal to the measured most-amplified disturbance frequency at $R = 1585$ in experiment S3. Computations are presented for two different streamwise velocity initial amplitudes, where $\tilde{u}_0$ refers to the root-mean-square of the streamwise velocity disturbance normalized by the free-stream velocity. In the left plot of figure 4, good agreement is observed between the frequencies
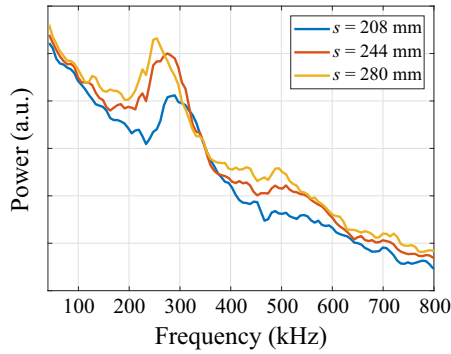
Figure 3. Spectra computed using reconstructed time signals from schlieren visualizations from experiment S3 at three different streamwise locations.
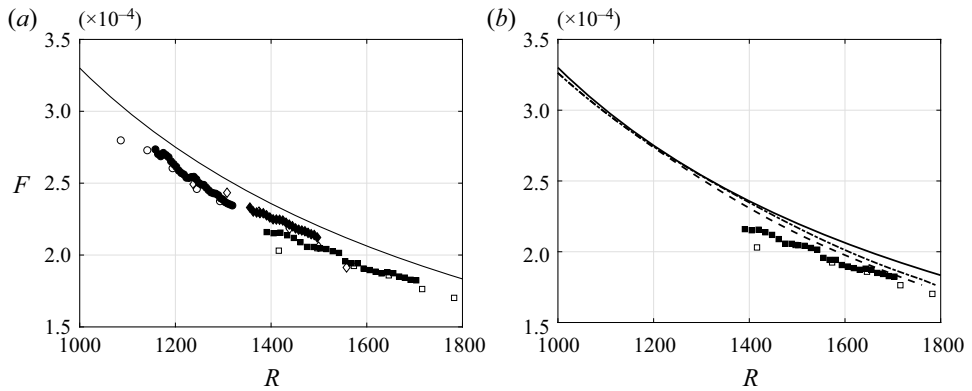

Figure 4. Most-amplified second-mode frequencies. (*a*) Experimental results for S1, S2, S3 shown with LPSE results. (*b*) Experimental results for S3 shown with LPSE results and NPSE results computed for disturbances with different streamwise velocity initial amplitudes. The data correspond to: (-◯-), S1; (-◇-), S2; (-▢-), S3; (–), LPSE; (- ·), NPSE, $\tilde{u}_0 = 5 \times 10^{-4}$; (- -), NPSE, $\tilde{u}_0 = 1 \times 10^{-3}$. Filled symbols are schlieren measurements, while open symbols are PCB measurements.

measured using the schlieren visualizations and PCB sensors. Across the measurement region, the LPSE overpredict the frequencies by approximately 5 %. In figure 4(*b*) it is observed that the addition of nonlinear effects in the NPSE computation leads to better agreement between the measurements and computations, as increasing the initial disturbance amplitude decreases the most-amplified second-mode frequencies. It is also noted that slight misalignment of the cone from zero incidence, but within the model installation accuracy of $\pm 0.5°$, may also contribute to a change in the experimentally observed second-mode frequencies and cause disagreement between the measured and computed results (see, for example, Hofferth, Humble & Floryan 2013).

Maximum N factors are computed here as

$$N(f_{max}, s_i) = \tfrac{1}{2} \ln(\text{PSD}(f_{max}, s_i)) + c, \tag{3.3}$$

where $\text{PSD}(f_{max}, s_i)$ is defined as the peak power of the most-amplified second-mode frequency at streamwise location s_i, and c is the vertical intercept identified by vertically shifting the schlieren measurements to match the LPSE curve. This vertical shift is required as the most upstream measurement location of the schlieren visualizations is
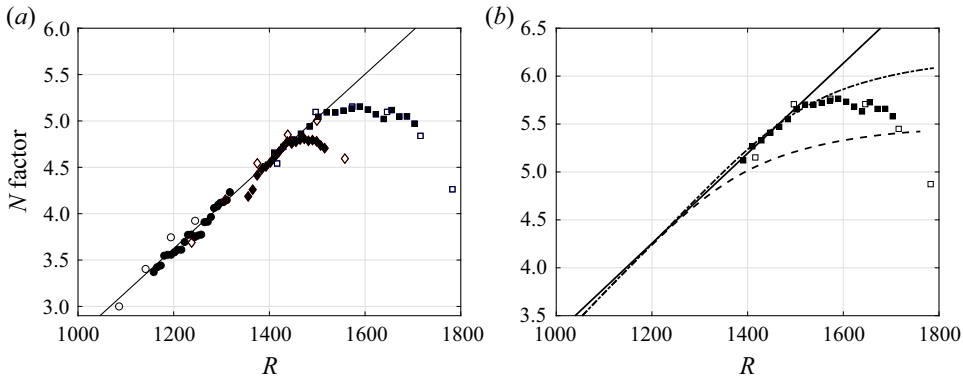
936 A39-8

Figure 5. Integrated amplification rates. (*a*) Experimental results for S1, S2, S3 shown with LPSE results. (*b*) Experimental results for S3 shown with LPSE results and NPSE results computed for disturbances with different streamwise velocity initial amplitudes. The data correspond to: (-○-), S1; (-◇-), S2; (-□-), S3; (–), LPSE; (- ·), NPSE, $\tilde{u}_0 = 5 \times 10^{-4}$; (- -), NPSE, $\tilde{u}_0 = 1 \times 10^{-3}$. Filled symbols are schlieren measurements, while open symbols are PCB measurements.

downstream of the second-mode neutral point; thus, although the relative growth of the wave amplitudes can be derived from the schlieren data, the absolute value of the *N* factors is meaningless without anchoring to the LPSE results. A different value of *c* is required for each individual run condition in order to match the LPSE curve. Calculating the growth rate by comparing amplitudes between two downstream locations is made possible by assuming that the change in boundary-layer height is negligible between the measurement locations. While not strictly true, Dunn & Lin (1955) showed this assumption to be valid to leading asymptotic approximation. Computation of the slope of the linear portion of the schlieren *N*-factor curve, i.e. the non-dimensional amplification rate, is performed using a weighted least-squares method in which the data points are weighed proportionally to their corresponding wave amplitudes.

Figure 5 presents the measured and computed *N* factors using the same convention as figure 4. The NPSE *N* factors presented in figure 5(*b*) are computed based on the disturbance pressure signature at the wall, p'_{wall}. Beginning our discussion with figure 5(*a*), the slope of the schlieren-derived maximum *N* factors in the linear-growth regime is $dN/dR = 5.05 \times 10^{-3}$, approximately 10 % higher than the slope of $dN/dR = 4.65 \times 10^{-3}$ computed from the LPSE. In agreement with the predictions of Mack (1975), the slope of the present Mach-6 experiments is approximately 60 % higher than that measured by Kennedy *et al.* (2018) on a 7° cone in a Mach-14 free stream using similar techniques. In addition to the linear growth for all conditions, nonlinear growth and saturation are observed for experiments S2 and S3. Deviation from the linear-growth regime and saturation occurs at a lower stability Reynolds number for experiment S2; this is consistent with the observations of Marineau *et al.* (2019), who found an increase in transition *N* factor with an increase in Re/m due to A_0 scaling as $(Re/m)^{-1}$. Figure 5(*b*) shows the *N* factors computed using the NPSE results and measured data for experiment S3. By fitting the critical stability Reynolds number, it is observed that the experimental measurements match most closely with the NPSE results computed using a disturbance with an initial streamwise perturbation velocity of 5×10^{-4}. The rapid saturation of the waves in the experimental data is likely due to secondary instabilities of the planar waves and subsequent breakdown that is not captured in the NPSE results (as these do not include three-dimensional effects). It is also noted that the accuracy of the line-of-sight integrated schlieren measurements become questionable near breakdown because of
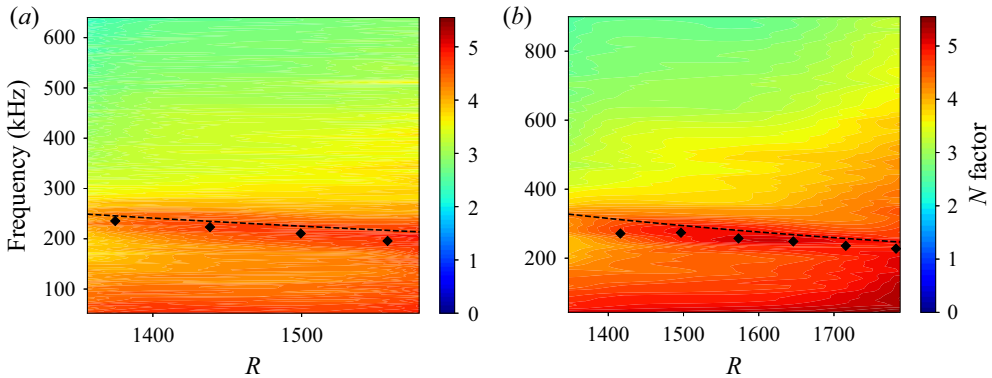
Figure 6. Plots of N factors computed as a function of frequency and stability Reynolds number: (*a*) experiment S2, (*b*) experiment S3. The black diamonds and the dashed lines represent PCB-derived and LPSE-derived most-amplified second-mode frequencies, respectively.

three-dimensional effects, and the free-stream noise environment can significantly affect the breakdown process.

In figure 6, schlieren-derived N factors are presented as functions of both frequency and stability Reynolds number for the two higher unit-Reynolds-number cases. Strictly speaking, the definition of the N factor presented in (3.3) implicitly assumes that the disturbance initial amplitudes are constant across the range of examined frequencies, i.e. a single value of the constant c; however, both measurements and simulations (Duan *et al.* 2019) have shown that free-stream disturbance amplitudes in conventional hypersonic tunnels such as the present facility are highly frequency dependent. Thus, direct comparisons of the *N*-factor magnitudes of, for example, the fundamental second-mode frequency, f_0, and harmonic content should be avoided, though the assumption should hold true over narrow ranges of frequencies. Nevertheless, qualitative assessment of harmonic presence is still meaningful. For experiment S2, a first harmonic becomes clearly present at $R \approx 1440$, approximately the same stability Reynolds number at which the maximum N factors deviate from the linear-growth regime in figure 5. A similar relationship of first harmonic growth and deviation of the maximum N factors from the linear regime is observed for experiment S3. Minimal power is observed at harmonic frequencies greater than $2f_0$ in either case.

3.1.1. *Bicoherence*

The presence of higher harmonics and nonlinear growth in experiments S2 and S3 motivates the examination of their origin. Nonlinear interactions in second-mode waves have previously been investigated by computing the measured signal bicoherence (Chokani 2005; Bountin, Shiplyuk & Maslov 2008). The method quantifies quadratic phase locking between various frequencies present in the signal to identify the origin of nonlinear phenomenon and differentiate spontaneously excited content from content generated by nonlinear interactions. In the present work, following the formulation of Kim & Powers (1979), the discrete bicoherence is computed as

$$b^2(f_1, f_2) = \frac{\left| \dfrac{1}{M} \sum\limits_{i=1}^{M} X(f_1)^{(i)} X(f_2)^{(i)} X^*(f_1 + f_2)^{(i)} \right|^2}{\left[\dfrac{1}{M} \sum\limits_{i=1}^{M} |X(f_1)^{(i)} X(f_2)^{(i)}|^2 \right] \left[\dfrac{1}{M} \sum\limits_{i=1}^{M} |X(f_1 + f_2)^{(i)}|^2 \right]}, \quad (3.4)$$
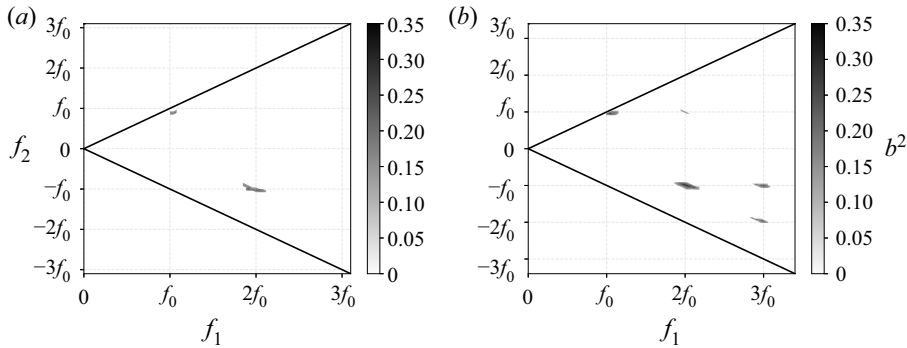
Figure 7. Bicoherence values computed from the schlieren time-reconstructed signals from experiment S3: (*a*) $R = 1484$, (*b*) $R = 1550$.

where $X(f)$ is the Fourier transform of a segment of the time series record, M is the number of signal segments and * indicates the complex conjugate. The b^2 value is bounded by 0 and 1, these two extremes indicating no phase coupling (spontaneous excitation) and complete phase locking, respectively. In practice, noise in experimentally obtained signals reduces the upper bicoherence to a value less than 1 (Kimmel & Kendall 1991).

In figure 7 we show the bicoherence computed from the calibrated time-reconstructed schlieren signals from experiment S3 at two streamwise locations. At the first location, just upstream of the deviation point of the maximum N factor from the linear part of the curve in figure 5, we observe phase locking of content at the fundamental disturbance frequency, $f_0 \approx 240$ kHz, to generate a first harmonic, $2f_0$, through a sum interaction at $f_0 + f_0 \rightarrow 2f_0$, and a difference interaction at $2f_0 - f_0 \rightarrow f_0$. Farther downstream at $R = 1550$ (right plot), at which point the waves have just entered the nonlinear-growth regime as indicated by the maximum N-factor curve, we observe the presence of additional interactions at $2f_0 + f_0 \rightarrow 3f_0$, $3f_0 - f_0 \rightarrow 2f_0$ and $3f_0 - 2f_0 \rightarrow f_0$ (with f_0 now having decreased to approximately 230 kHz due to boundary-layer growth). These interactions indicate energy exchange through phase locking between fundamental, first and second harmonic frequency content just prior to breakdown. The power of the strongest sum interaction, $f_0 + f_0 \rightarrow 2f_0$, increases between the two locations examined here from 0.24 to a maximum value of 0.34. As the waves mature further and reach breakdown, the power and number of nonlinear interactions present in the bicoherence plots decrease until no quadratic interactions remain.

Consistent with the observations of Kennedy *et al.* (2018) at Mach 14, nonlinear interactions involving content at a particular harmonic frequency appear upstream of the location where power appears at that frequency in the power spectrum; furthermore, such interactions reach a maximum value upstream of where the power spectral density (PSD) at that frequency reaches a maximum, indicating that the strongest phase locking precedes the location of maximum amplitude of the harmonic content (i.e. the bicoherence magnitude is linked to the harmonic growth rate rather than absolute power in the PSD). For example, in experiment S3, interactions involving $2f_0$ reach a maximum value at approximately $R = 1550$ shown in figure 7(*b*) and begin to decrease downstream, whereas the power observed at this frequency in the PSD continues to increase with increasing streamwise location. Additionally, interactions involving $3f_0$ are identified, though minimal power is observed at this frequency in the PSD. No significant interactions were observed involving frequency content greater than $3f_0$; this is in contrast to the
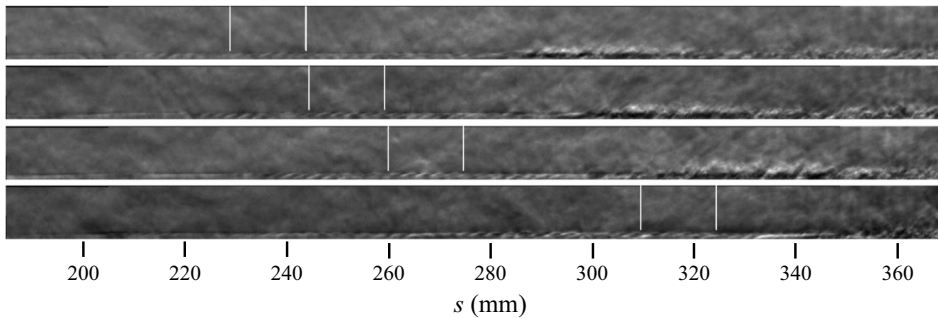
Figure 8. Enhanced schlieren visualizations showing the evolution of a single second-mode wavepacket from experiment S3. The first image is recorded at time t_0, with subsequent images at $t_0 + 21.3\ \mu s$, $t_0 + 42.6\ \mu s$ and $t_0 + 115.0\ \mu s$. The markers show the approximate extent of the wavepacket in the first image and have been translated downstream in the subsequent images according to the mean propagation speed.

Mach-14 results of Kennedy *et al.* (2018) which revealed interactions involving frequencies up to $5f_0$.

3.1.2. *Circumferential extent of wavepackets*

The circumferential extent of the second-mode waves can be examined using the three-sensor spanwise array located at $s = 316$ mm. For each experiment, the coherence as a function of frequency is computed between each of the sensors in the array over the second steady-flow period, generating coherence measurements for circumferential separations of 5.72 mm and 11.43 mm. Following Kimmel, Demetriades & Donaldson (1996), a coherence cutoff criterion of 0.2 is used to define the pressure disturbance width.

For the sharp-nose experiment with the lowest unit-Reynolds-number condition, S1, the maximum signal coherence is greater than 0.2 between the two outermost sensors. The higher-Reynolds-number condition S2 and S3 signals have maximum coherence values greater than this cutoff value between the centre-line sensor and outer sensor but less than it between the two outermost sensors. By fitting a Gaussian to the three circumferential measurement locations (using a coherence value of 1 at the centre of the array), the extents are estimated as 4.20δ for experiment S1, 3.16δ for experiment S2 and 3.11δ for experiment S3, where δ is the local boundary-layer thickness. These results are similar to those reported by Kimmel *et al.* (1996), showing the normalized circumferential pressure footprint of the waves to be limited to a few boundary-layer thicknesses and decrease with increasing unit Reynolds number.

3.2. *Individual wavepacket development*

Insights into individual second-mode wavepacket development are made possible by the high frame rates of the schlieren system with respect to the fundamental second-mode frequency, allowing for a single wavepacket to be captured in approximately 40 consecutive frames. In figure 8 a single second-mode wavepacket from the highest unit-Reynolds-number sharp-nose experiment S3 is shown. Presented in figure 9 is a synthetic schlieren image generated using the NPSE computed for the same conditions as this experiment. Following Laurence *et al.* (2016) and Kennedy *et al.* (2018), in figure 10 we plot the wavepacket energy distribution at different heights above the cone surface for the images shown in figure 8. In the earliest stage of development shown in this figure (top left), the wavepacket contains fundamental frequency content at 270 kHz concentrated
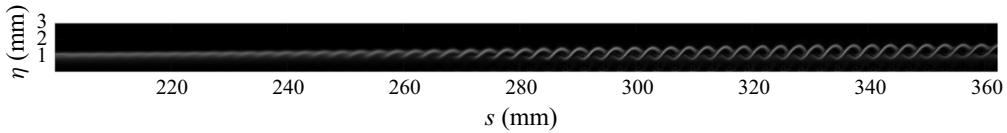
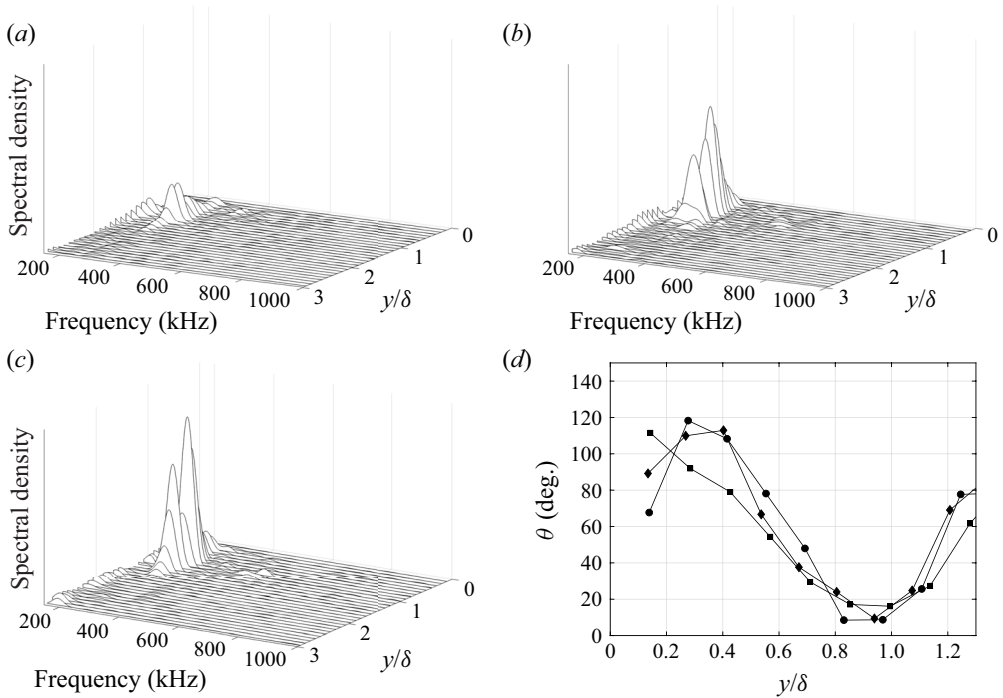Figure 9. Synthetic schlieren image computed using NPSE at the same free-stream conditions as experiment S3.

Figure 10. Wall-normal power spectral densities at times: (*a*) t_0, $R = 1484$; (*b*) $t_0 + 21.3$ μs, $R = 1532$; (*c*) $t_0 + 42.6$ μs, $R = 1578$. (*d*) Structure angles of the wave fundamental frequency content at different points of development: (-□-) t_0; (-○-) $t_0 + 21.3$ μs; (-◇-) $t_0 + 42.6$ μs.

between $y/\delta = 0.8$ and 1.1. The fundamental content is significantly amplified by the next downstream station shown in figure 10(*b*), where we also observe growth of a second peak at the outer edge of the boundary layer. By $t_0 + 42.6$ μs ($R = 1578$), the fundamental content has distinct peaks at 0.88δ and 1.08δ, and weak first harmonic content in the 520 kHz range becomes visible at the same wall-normal locations. Comparing to the time-averaged maximum N factors of figure 5, the amplification of the outer peak and of harmonic power roughly coincide with the location of deviation from the linear-growth regime. Further downstream, the fundamental and harmonic peaks decrease in power until no distinct peaks remain and the wavepacket is on the verge of full breakdown to turbulence, as seen in the final image of figure 8. Experiment S3 is chosen here to demonstrate the wavepacket development as it contains the most mature waves, although it is noted that the waves from experiment S2 evolve similarly, with a two-profile peak in the fundamental content observed for more mature waves. These observations are also qualitatively consistent with the findings of Kennedy *et al.* (2017) for mature second-mode wavepackets developing in a Mach-14 free stream. No near-wall peak such as that observed
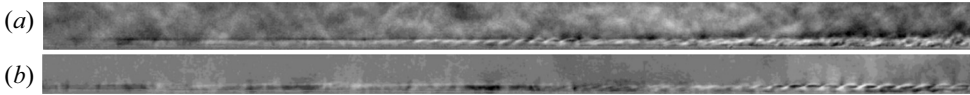
Figure 11. Enhanced schlieren visualizations generated by subtracting a mean flow-on image from the image of interest. Images correspond to nose-tip-radius configurations of (*a*) 0.508 mm, (*b*) 1.524 mm.

by Laurence *et al.* (2016) at higher enthalpy conditions is observed in any of the present wavepackets, perhaps a result of the higher T_w/T_{aw} value here.

Next, we consider the inclination of the structures in the *s*–*y* plane (often referred to as the structure angle), θ, at different stages of development. The fundamental structure angle is calculated by first bandpass filtering the signal reconstructed at each wall-normal location around the fundamental second-mode frequency. Cross-correlation coefficients for vertically separated signals are computed for various streamwise displacements, and the displacement corresponding to the highest-valued coefficient is used to find the value of θ. The lower right panel of figure 10 presents structure angles computed for the wavepackets shown in figure 8. In general, the fundamental content of the waves is tilted slightly upstream into the flow in the near-wall region, then rapidly curves towards the direction of the flow moving closer to the boundary-layer edge. The two more mature wavepacket stages shown in the second and third images of figure 8 take on a similar profile, reaching a maximum angle of 110°–120° between $y/\delta = 0.2$–0.4. The minimum angles lie in the range 9°–15° near the edge of the boundary layer. Similar measurements by Kimmel & Kendall (1991), Parziale (2013) and Laurence *et al.* (2016) cite minimum angles in the 10°–15° range.

4. Instability development over blunt-nose cone configurations

We now turn our attention to the instability development for the nose tips of finite-radius bluntnesses. In general, second-mode waves remain the most visible features within the schlieren visualizations for the 0.508 mm and 1.524 mm nose-tip-radius configurations, although extremely weak elongated features extending above the boundary layer begin to appear upstream of the entropy-layer swallowing length for the 1.524 mm case. For the 2.54 mm and 5.08 mm cases, second-mode waves are no longer visible within the boundary layer and instead elongated features believed to be associated with non-modal growth appear. The visualized features for a given model configuration and free-stream condition appear to be primarily dependent on the viewing location with respect to the entropy-layer swallowing length. Computational (Paredes *et al.* 2019*b*) and experimental (Grossir, Pinna & Chazot 2019) data have shown that both non-modal features and second-mode waves can exist in the vicinity of the entropy-layer swallowing length. Because of the constraints of our visualization region, however, in no case were we able to capture enough of the cone to visualize both types of features for the same condition. We will thus explore the instability mechanisms separately. First, we focus on the cases where second-mode waves are clearly visible within the boundary layer, and then turn our attention to characterizing the non-modal features present for the blunter cases.

4.1. *Second-mode dominated regime*

For cone configurations with nose-tip radii of 1.524 mm and less, the same temporal reconstruction technique as used in the sharp-nose case is applied and a similar analysis is performed. Sample images from experiments B1 and B2 are shown in figure 11.
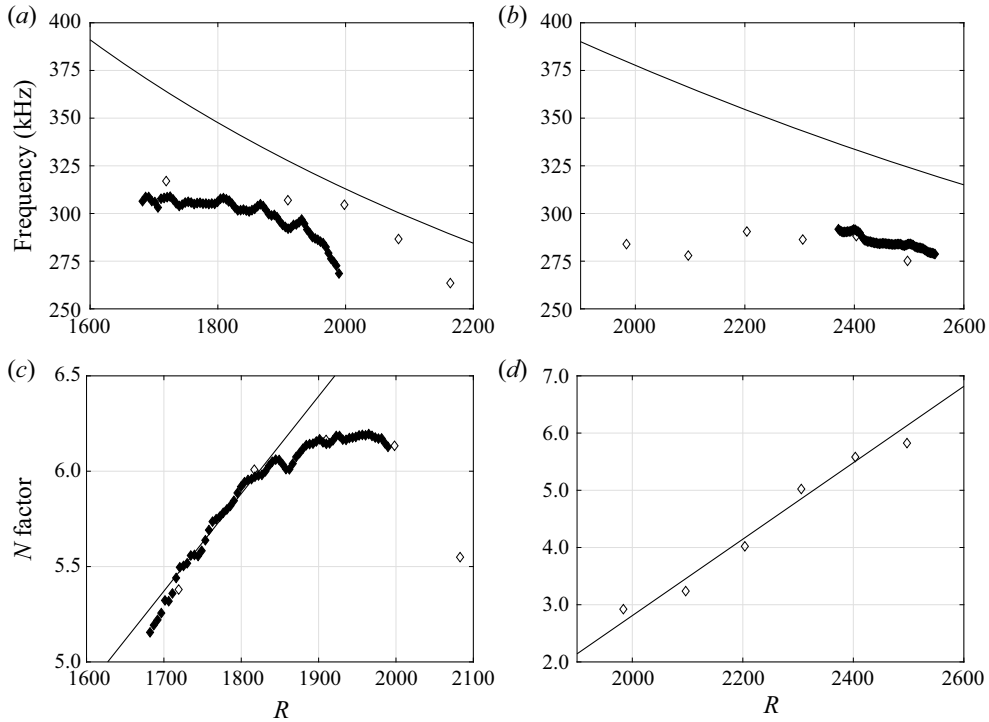
Figure 12. (*a*,*c*) Experiment B1. (*b*,*d*) Experiment B2. (*a*,*b*) Most-amplified second-mode frequencies. (*c*,*d*) Plots of *N* factors. Filled symbols are schlieren measurements; open symbols are PCB measurements; lines are LPSE results.

In figure 12 we show the most-amplified second-mode frequencies and their associated *N* factors for experiments B1 and B2. Beginning with experiment B1, the frequencies computed by the LPSE are observed to be 10–20 % higher than the PCB and schlieren frequencies across the entire measurement range. Good agreement is observed between the PCB and schlieren measurements in the upstream portion of the visualization region. In the linear-growth regime, the slope of the *N*-factor curve computed from the schlieren is within 15 % of that computed from the LPSE. Deviation from the linear curve occurs at approximately $R = 1820$ for both the schlieren and PCB measurements, resulting in a transition *N* factor of 6.2. The higher transition *N* factor here compared with the sharp-nose results is believed to be a combination of the higher unit-Reynolds-number free stream and higher most-amplified second-mode frequencies. Longer wavelength features similar to those observed by Casper *et al.* (2016) in schlieren visualizations over a $7°$ half-angle cone in a Mach-5 free stream also appear. Casper *et al.* (2016) attributed these low frequency disturbances to the first mode, and, considering the edge Mach numbers of 3.4–3.7 in the present experiments, it may be expected to be present to some extent here as well. While the direct numerical simulations (DNS) of Hader, Deng & Fasel (2021) found the first mode to influence the transition process on a sharp-nose cone at Mach 5, a bispectral analysis of the present experiments did not indicate any significant nonlinear interactions between the lower-frequency and second-mode content. Turning to the results of experiment B2 (right plots of figure 12), a significant discrepancy is observed between the LPSE frequencies and those measured from the PCB and schlieren data. The greatest deviation between the LPSE and PCB measurements is observed

Figure 13. Enhanced schlieren visualization generated by subtracting a mean flow-on image from the image of interest for the 2.540 mm nose-tip-radius configuration.
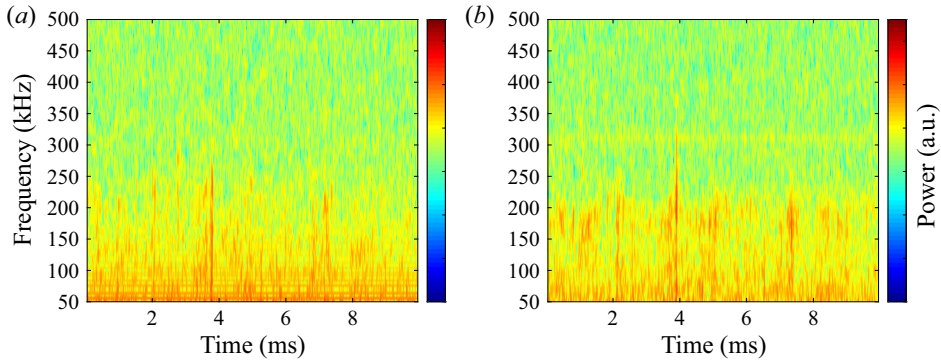

Figure 14. Short-time Fourier transforms computed from PCB signals at (*a*) $s = 241$ mm, (*b*) $s = 341$ mm for experiment B4.

upstream where the maximum frequency is difficult to extract due to the PCB signal being weak, while downstream the PCB and schlieren frequencies are roughly within 10 % of those of the LPSE. Additionally, the PCB sensors have a resonant frequency at roughly 300 kHz making identification of the peak frequency in the upstream sensors difficult. The reduced value of the measured frequencies compared with the computed frequencies is expected due to the finite initial amplitudes of the experimentally measured waves. The low signal-to-noise ratio in the upstream portion of the viewing area hindered the ability to compute N factors from the schlieren measurements, but the PCB data agree well with the computation in figure 12(*d*).

4.2. *Non-modal instability features*

The unsteady elongated features first appear consistently in the visualizations of the 2.54 mm nose-tip-radius configuration as shown in figure 13, and are frequently present for the 5.08 mm configuration. The following characterization focuses on the latter case as the features are significantly more visible due to both the image magnification and viewing location. For both experiments with this nose-tip bluntness (B4 and B5), the predicted entropy-layer swallowing length is roughly 1.25 m past the end of the cone model, and no significant difference in visual structure is observed between the features of the two slightly different experimental conditions. In general, the features extend above the visual edge of the boundary layer and are similar in appearance to those captured in the images of Grossir *et al.* (2019). In contrast to the conditions where second-mode waves are present, no sharp peaks appear in the PCB power spectra computed over the entire test time; however, as seen in figure 14, isolated bursts of high-frequency (150–250 kHz) pressure content appear in the PCB signals resulting in a broad peak in the mean frequency spectra shown in figure 15. The peaks observed at approximately 300 kHz are most likely artifacts of the resonant frequency of the PCB sensors, and the spectra of the signals measured by the sensor at $s = 341$ mm contain significant noise at frequencies greater than 200 kHz. By matching the timestamps between the images and PCB array, it is possible to
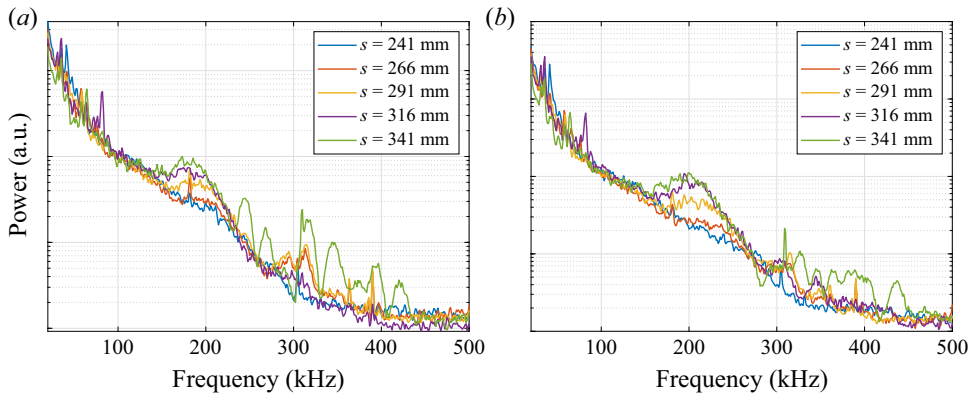
Figure 15. Mean spectra computed from PCB signals for (*a*) experiment B4, (*b*) experiment B5.

unambiguously associate the visible non-modal features with the high-frequency bursts in the PCB signals.

General observations are made by analysing 15 clearly visible non-modal features present for experiments B4 and B5. These features develop slowly when compared with the rapid growth and breakdown of the second-mode instability waves. In presenting typical characteristics, we first consider the overall shape of such features. Focusing on figures 16 and 17, they are nearly parallel to the cone surface at the trailing (i.e. upstream in the mean flow) edge and then gradually curve away from the surface. As the features propagate across the visualization region, the portion at the leading edge rotates downward towards the cone surface, resulting in a decrease in the inclination angle and flattening of the structure. The maximum inclination angle lies between $13°$–$19°$ when the feature is at the most upstream end of the viewing area and decreases to $8°$–$14°$ once it has propagated to the most downstream visible location. Figure 18 shows this evolution in feature shape by presenting the profile of maximum pixel intensity within a single non-modal feature at four sequential timesteps (separated by $21.3\ \mu$s) from experiment B4. Select features such as that shown in figure 16(*h*) are also observed to exhibit a region of high curvature near the leading edge (downstream end). In general, the features extend $2\delta - 3\delta$ above the cone surface, and the strongest density gradients are observed at a wall-normal height of $1\delta - 2.5\delta$. The linear non-modal analysis of planar waves of the B4 configuration is shown in figure 19. The linearly optimal perturbations that result in maximum Mack's energy gain, G_E, at a specified downstream location are computed with the variational formulation based on the HLNSE (Paredes *et al.* 2019*b*). The inflow location is selected at $s_0 = 24$ mm, close to the nose-tip juncture. Figure 19(*a*) shows the dependency of the optimization outflow location with respect to the disturbance frequency for maximum energy gain. Figure 19(*b*) shows the optimal energy gain in terms of the N factor calculated as $N_E = 0.5 \log(G_E)$, corresponding to the outflow locations for maximum energy growth of figure 19(*a*) for the selected frequencies. The outflow location and disturbance frequencies that correspond to the maximum energy gain are $s_1 = 305$ mm and $f = 125$ kHz. The corresponding inflow disturbance profile with the parameters corresponding to maximum energy gain (i.e. $s_0 = 24$ mm, $s_1 = 305$ mm and $f = 125$ kHz) is used as the inflow condition for the parabolic integration of the NPSE with an initial amplitude of $|T'|_{rms}/T_\infty = 0.002$. The synthetic schlieren image of the disturbance is shown in figure 20. Comparison of DNS and NPSE results of the nonlinear evolution of non-modal waves in a blunt cone was presented by Paredes *et al.* (2020). As
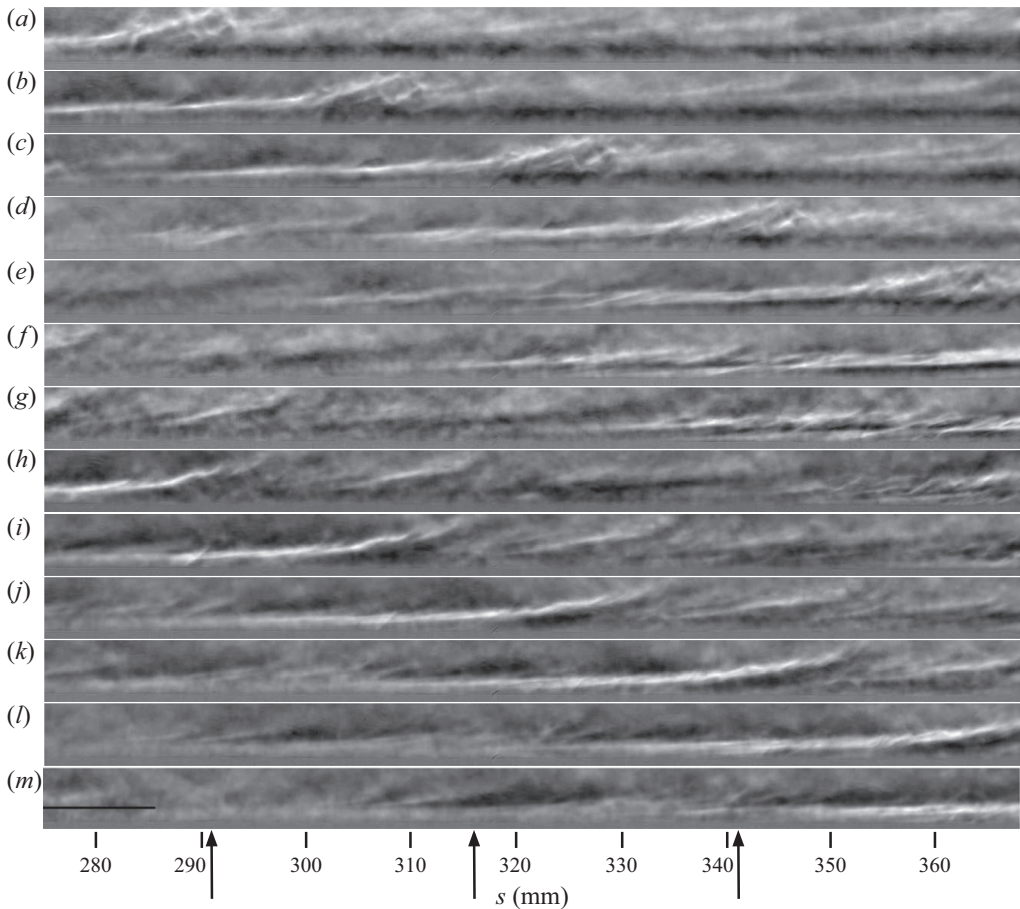
Figure 16. Enhanced visualization sequence from experiment B4 ($R_N = 5.08$ mm). The top image corresponds to time t_0 with subsequent images separated by 21.3 µs (i.e. every fifth image shown). Black arrows indicate the streamwise locations of the three most downstream PCB sensors ($s = 291$ mm, $s = 316$ mm and $s = 341$ mm). The black horizontal line in the final image indicates the computed boundary-layer thickness.

observed by comparing figures 17 and 20, the individual experimental and computation features are very similar in appearance and share, for example, the gradual flattening of the structure with downstream propagation, indicating that they are likely the same features. While the spatial periodicity of the features in figure 20 is not apparent in figure 17, this is not necessarily expected in the experimental measurements as the N factor is fairly flat over a wide range of frequencies in figure 19(*b*) and the computations of Paredes *et al.* (2019*c*) predict the non-modal features to exhibit amplification over a broad range of frequencies. The inclination angles of the computed features lie slightly below the lower end of the experimentally observed range with values of approximately $11°$ and $7°$ at the most upstream and downstream streamwise locations.

In figure 21 we show the streamwise PCB pressure traces corresponding to the image sequences presented in figures 16 and 17. Two distinct instability features are observed in the lower unit-Reynolds-number experiment B4 shown in figure 16; their associated pressure footprints are seen in the most upstream PCB sensor at $t - t_0 = 95$ µs and $t - t_0 = 240$ µs. As the feature passes over the sensor, a slight rise followed by several high-frequency (several hundred kHz) oscillations is characteristic of the pressure
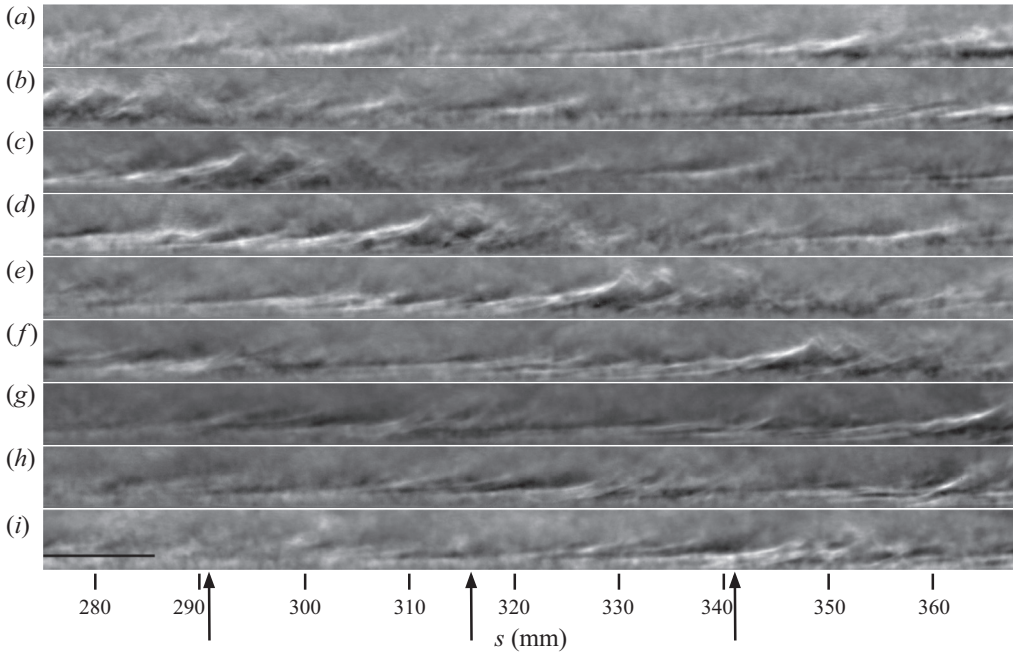
Figure 17. Enhanced visualization sequence from experiment B5 ($R_N = 5.08$ mm). The top image corresponds to time t_0 with subsequent images separated by 21.3 μs (i.e. every fifth image shown). Black arrows indicate the streamwise locations of the three most downstream PCB sensors ($s = 291$, $s = 316$ and $s = 341$ mm). The black horizontal line in the final image indicates the computed boundary-layer thickness.
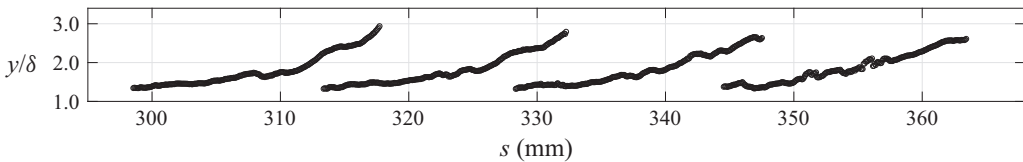

Figure 18. Profile of maximum pixel intensity extracted for the feature shown in images (i)–(l) of figure 16.
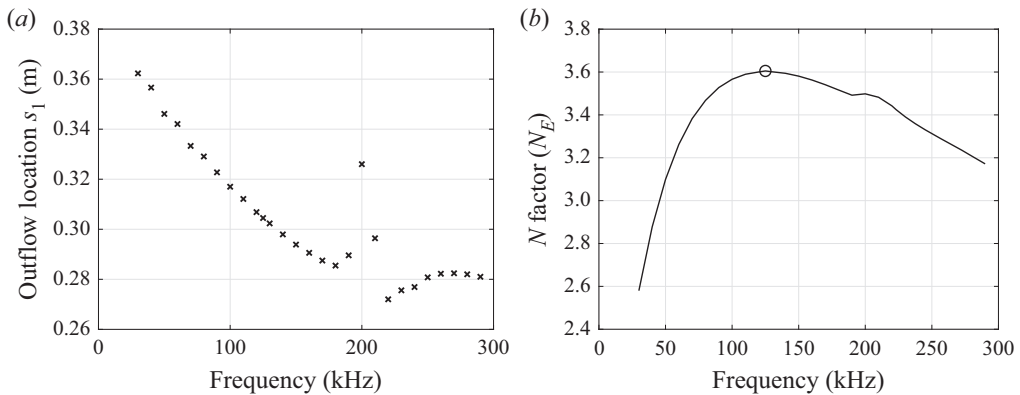

Figure 19. Characteristics of the optimal perturbation used as the inflow condition for the NPSE calculations. (a) Outflow location (s_1) for maximum energy gain disturbance frequency; (b) N factor computed using the Mack energy norm versus disturbance frequency. The circle indicates the maximum N_E.
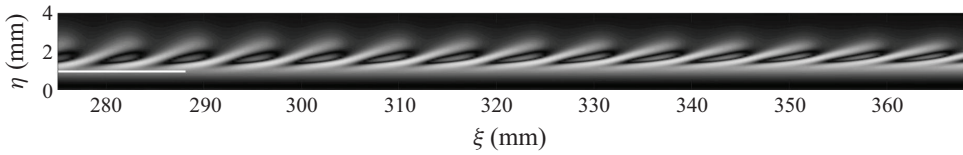
Figure 20. Synthetic schlieren computed for the same free-stream conditions as experiment B5. The white horizontal line indicates the computed boundary-layer thickness.
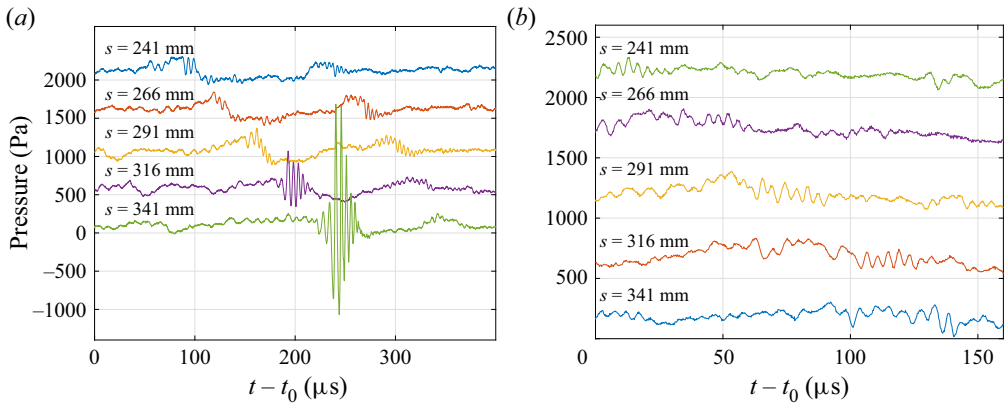

Figure 21. Plots of PCB pressure traces at different streamwise locations: (*a*) experiment B4, (*b*) experiment B5. The traces are vertically offset according to the measurement coordinate.

disturbance at the wall; a similar pressure disturbance with a frequency of approximately 250 kHz is observed in the most upstream sensor for the experiment B5 disturbance. The two disturbances for experiment B4 in the left plot of figure 21 have a similar profile until $s = 316$ mm, by which point the high-frequency content in the earlier disturbance has been significantly amplified and that of the later disturbance attenuated. By $s = 341$ mm, the earlier disturbance contains extremely strong content with a frequency of approximately 182 kHz, and the later disturbance is almost completely attenuated. The rapid amplification of the earlier disturbance recorded at the two most downstream sensors is an anomalous case; all other pressure disturbances associated with non-modal features appear similar in shape and magnitude up through the sensor at $s = 291$ mm and see minimal amplification in the more downstream sensors. Nonetheless, this unique disturbance is worth noting, as it appears visually similar to the other instability features and no obvious high-frequency signal appeared in the schlieren images corresponding to these features. In general, the high-frequency pressure disturbances generated by the non-modal features of experiment B5 exhibit slightly higher frequencies than those of experiment B4. Given the inversely proportional relationship between the second-mode fundamental frequencies and boundary-layer thickness, this may indicate that the high-frequency pressure disturbances associated with the trailing edge of the non-modal features are related to the second mode.

In figure 22 we show the pressure signals recorded by the PCB spanwise array during the time period of the two image sequences. The circumferential extent of the high-frequency pressure disturbance appears limited, typically encompassing just two of the laterally offset sensors with minimal content at the third. Beginning with B4, the high-frequency disturbance at $t - t_0 = 200$ µs is strongest in the centre sensor, with a
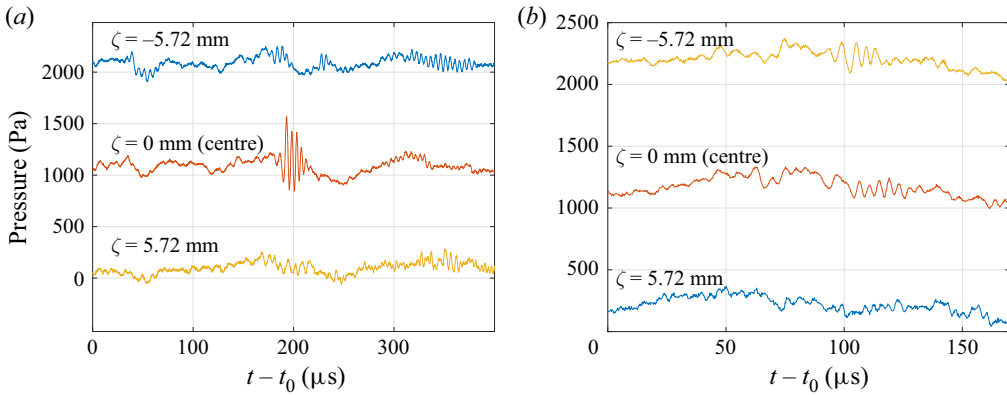
Figure 22. Plots of PCB pressure traces at different spanwise locations: (*a*) experiment B4, (*b*) experiment B5. The traces are vertically offset according to the measurement coordinate.

weak pressure disturbance present in the sensors located on either side at $\zeta = 5.72$ mm and $\zeta = -5.72$ mm (though this was an exceptional case). Weak content is also observed in the $\zeta = -5.72$ mm and $\zeta = 0$ sensor signals at $t - t_0 = 50$ μs and $t - t_0 = 340$ μs. For the B5 traces, the pressure disturbance at time $t - t_0 = 110$ μs is visible in both the $\zeta = -5.72$ mm and $\zeta = 0$ sensor, but minimal signature is observed in the $\zeta = 5.72$ mm sensor. For both experiments, the maximum coherence over all frequencies gives a magnitude-squared coherence estimate of 0.4–0.55 for adjacent sensors. Limited coherence ($\sim$0.1) is observed between the $\zeta = -5.72$ mm and $\zeta = 5.72$ mm sensor signals, though ambiguity remains in defining the features associated with non-modal growth using solely the pressure data because of the lack of a single distinguishing disturbance frequency. In terms of the local boundary-layer thickness computed from the DPLR mean-flow solution, the resulting spanwise extent of the high-frequency disturbances is of the order of $5\delta - 10\delta$.

Propagation speeds are computed by selecting a region of the feature located between the boundary-layer and entropy-layer edges and using a cross-correlation technique to identify the downstream propagation between sequential images, similar to calculations of the second-mode propagation speeds. The average speed and 95 % confidence interval calculated over 162 image pairs from experiment B4 is 780 ± 90.1 m s^{-1}; values calculated for experiment B5 also fall within this range. The edge velocities computed for these two conditions using the DPLR mean-flow solution are 761 m s^{-1} and 757 m s^{-1}, respectively, leading to a $u_{prop}/u_e = 1.03$. Slightly higher propagation velocities are expected given that the structures extend beyond the boundary-layer edge. Additionally, no clear regularity is observed in the spacing between features. We can identify two possibilities for this lack of clear frequency content: the instability features undergoing non-modal amplification are not associated with a single dominant frequency, or the reduced schlieren contrast resulting from the entropy layer combined with the integrated nature of the technique eliminates the ability to consistently identify features. A dominant disturbance frequency may, however, not be expected as the computational results of Paredes *et al.* (2019*b*) predict that the non-modal features exhibit amplification over a significantly broader range of frequencies than the second mode, with the most-amplified frequencies lying in the 100–800 kHz range depending on the cone model nose-tip radius and free-stream conditions. Free-stream noise levels may also play a role in which frequency disturbances become most amplified.

5. Conclusion

Second-mode instability waves and non-modal instability features are visualized and characterized using calibrated high-speed schlieren cinematography and PCB pressure sensor measurements, with results compared with those from PSE computations. The radius of the cone nose tip is the main parameter dictating which instability mechanisms dominate the flow close to the cone surface. As anticipated, for the sharp-nose model configurations, the second-mode instability is the dominant instability mechanism leading to boundary-layer transition. Good agreement is observed between the measurements and computations for the second-mode most-amplified frequencies and N factors. Several key differences are observed for the second-mode development in the present Mach-6 free stream compared with the previous results of Kennedy *et al.* (2018) in a Mach-14 free stream using the same measurement techniques. First, the slope of the maximum N-factor curve at Mach 6 is approximately 60 % greater than at Mach 14. Second, fewer nonlinear interactions involving higher harmonics are identified in the bicoherence results and PSDs at the lower Mach number. Significant differences in the free-stream noise spectrum, unit Reynolds numbers and Mach number between the relevant experimental facilities eliminate the ability to identify a single factor for the difference in development, but the reduced harmonic presence at the lower Mach number is noteworthy given the importance of nonlinear energy exchange within the wavepackets during the breakdown to transition. In line with previous literature, individual second-mode waves were found to have their highest power concentrated in the upper half of the boundary layer, and the waves exhibit a fairly limited circumferential extent of $3\delta - 4\delta$.

For blunt-nose tips, high-speed visualizations provide a comprehensive dataset, capturing the evolution of instability features between the boundary-layer and entropy-layer edges undergoing non-modal growth. The non-modal features appear clearly in the schlieren images captured using the two largest nose-tip-radius configurations, for which the visualization region is significantly upstream of the entropy-layer swallowing length. These features evolve slowly compared with the second-mode waves and appear to flatten as they propagate downstream. These elongated features are also observed in synthetic schlieren images generated from the PSE results computed at the same experimental conditions. High-frequency pressure oscillations are observed at the wall during the passage of the trailing edge of the non-modal features; this was somewhat unexpected based on the visualizations (in which high-frequency spatial content is not generally detected), but this signature provides a means to identify the presence of a non-modal feature based on surface measurements. The signature at the wall may serve as a guide for computational results in such cases, since not all of the different disturbances that can develop (i.e. planar and oblique waves of varying wavenumbers) penetrate the boundary layer (Paredes *et al.* 2019*b*). Finally, it is noted that for the blunted nose tip, the pressure oscillations exhibited a higher frequency at higher unit-Reynolds-number conditions; as this is the same behaviour expected of second-mode waves, this may suggest a connection between the two instability mechanisms.

Future work in this area should aim to comprehensively characterize the free-stream noise spectrum in the AFRL Ludwieg tube, as tunnel noise has been shown to play a role in instability development. Significant progress in focused laser differential interferometry (FLDI) (Parziale 2013; Settles & Fulghum 2016; Jewell *et al.* 2019) provides a promising path forward for non-intrusively measuring free-stream disturbances levels. A FLDI set-up with multiple streamwise interrogation probes could also be used to identify the streamwise coordinate where second-mode instability waves first begin to grow within the

boundary layer. Finally, experiments involving higher-Reynolds-number flows could allow for the direct observation of breakdown of the non-modal features.

Declaration of interests. The authors report no conflict of interest.

Author ORCIDs.

Richard E. Kennedy https://orcid.org/0000-0001-9816-2224;

Joseph S. Jewell https://orcid.org/0000-0002-4047-9998;

Pedro Paredes https://orcid.org/0000-0003-1890-1811;

Stuart J. Laurence https://orcid.org/0000-0001-8760-8366.

REFERENCES

BOUNTIN, D.A., SHIPLYUK, A.N. & MASLOV, A.A. 2008 Evolution of nonlinear processes in a hypersonic boundary layer on a sharp cone. *J. Fluid Mech.* **611**, 427–442.

CASPER, K.M., BERESCH, S.J., HENFLING, J.F., SPILLERS, R.W., PRUETT, B.O.M. & SCHNEIDER, S.P. 2016 Hypersonic wind-tunnel measurements of boundary-layer transition on a slender cone. *AIAA J.* **54** (4), 1250–1263.

CHOKANI, N. 2005 Nonlinear evolution of Mack modes in a hypersonic boundary layer. *Phys. Fluids* **17**, 014102.

DUAN, L., *et al.* 2019 Characterization of freestream disturbances in conventional hypersonic wind tunnels. *J. Spacecr. Rockets* **56** (2), 357–368.

DUNN, D.W. & LIN, C.C. 1955 On the stability of the laminar boundary layer in a compressible fluid. *J. Aeronaut. Sci.* **22** (7), 455–477.

GROSSIR, G., PINNA, F., BONUCCI, G., REGERT, T., RAMBAUD, P. & CHAZOT, O. 2014 Hypersonic boundary layer transition on a 7 degree half-angle cone at Mach 10. *AIAA Paper* 2014-2779.

GROSSIR, G., PINNA, F. & CHAZOT, O. 2019 Influence of nose-tip bluntness on conical boundary-layer instabilities at Mach 10. *AIAA J.* **57** (9), 3859–3873.

HADER, C., DENG, N. & FASEL, H.F. 2021 Direct numerical simulations of hypersonic boundary-layer transition for a straight cone at Mach 5. *AIAA Paper* 2021-0743.

HARGATHER, M.J. & SETTLES, G.S. 2012 A comparison of three quantitative schlieren techniques. *Opt. Lasers Engng* **50** (1), 8–17.

HOFFERTH, J.W., HUMBLE, R.A. & FLORYAN, D.C. 2013 High-bandwidth optical measurements of the second-mode instability in a Mach 6 quiet tunnel. *AIAA Paper* 2013-0378.

JEWELL, J.S. 2014 Boundary-layer transition on a slender cone in hypervelocity flow with real gas effects. PhD thesis, California Institute of Technology.

JEWELL, J.S., HAMEED, A., PARZIALE, N.J. & GOGINENI, S. 2019 Disturbance speed measurements in a circular jet via double focused laser differential interferometry. *AIAA Paper* 2019-2293.

JEWELL, J.S. & KIMMEL, R.L. 2017 Boundary-layer stability analysis for Stetson's Mach 6 blunt-cone experiments. *J. Spacecr. Rockets* **54** (1), 258–265.

JOHNSON, H.B. 2000 Thermochemical interactions in hypersonic boundary layer stability. PhD thesis, University of Minnesota.

JOHNSON, H.B. & CANDLER, G.V. 2005 Hypersonic boundary layer stability analysis using PSE-Chem. *AIAA Paper* 2005-5023.

JOHNSON, H.B., SEIPP, T.G. & CANDLER, G.V. 1998 Numerical study of hypersonic reacting boundary layer transition on cones. *Phys. Fluids* **10**, 2676–2685.

KENNEDY, R.E. 2019 An experimental investigation of hypersonic boundary-layer transition on sharp and blunt slender cones. PhD thesis, University of Maryland, College Park.

KENNEDY, R.E., LAURENCE, S.J., SMITH, M.S. & MARINEAU, E.C. 2017 Hypersonic boundary-layer transition features from high-speed schlieren images. *AIAA Paper* 2017-1683.

KENNEDY, R.E., LAURENCE, S.J., SMITH, M.S. & MARINEAU, E.C. 2018 Investigation of the second-mode instability at Mach 14 using calibrated schlieren. *J. Fluid Mech.* **845**, R2.

KIM, Y.C. & POWERS, E.J. 1979 Digital bispectral analysis and its applications to nonlinear wave interactions. *IEEE Trans. Plasma Sci.* **7** (2), 120–131.

KIMMEL, R.L., BORG, M.P, JEWELL, J.S., LAM, K.Y., BOWERSOX, R.D., SRINIVASAN, R., FUCHS, S. & MOONEY, T. 2017 AFRL Ludwieg tube initial performance. *AIAA Paper* 2017-0102.

KIMMEL, R.L., DEMETRIADES, A. & DONALDSON, J.C. 1996 Space-time correlation measurements in a hypersonic transitional boundary layer. *AIAA J.* **34** (12), 2484–2489.

KIMMEL, R.L. & KENDALL, J.M. 1991 Nonlinear disturbances in a hypersonic boundary layer. *AIAA Paper* 1991-0320.

LAURENCE, S.J., WAGNER, A. & HANNEMANN, K. 2014 Schlieren-based techniques for investigating instability development and transition in a hypersonic boundary layer. *Exp. Fluids* **55**, 1–17.

LAURENCE, S.J., WAGNER, A. & HANNEMANN, K. 2016 Experimental study of instability growth and breakdown in a hypersonic boundary layer using high-speed schlieren visualization. *J. Fluid Mech.* **797**, 471–501.

MACK, L.M. 1975 Linear stability theory and the problem of supersonic boundary-layer transition. *AIAA J.* **13** (3), 278–289.

MARINEAU, E.C., GROSSIR, G., WAGNER, A., LEINEMANN, M., RADESPIEL, R., TANNO, H., CHYNOWETH, B.C., SCHNEIDER, S.P., WAGNILD, R.M. & CASPER, K.M. 2019 Analysis of second-mode amplitudes on sharp cones in hypersonic wind tunnels. *J. Spacecr. Rockets* **56** (2), 307–318.

MARINEAU, E.C., MORARU, G. & DANIEL, D.T. 2017 Sharp cone boundary-layer transition and stability at Mach 14. *AIAA Paper* 2017-0766.

MARINEAU, E.C., MORARU, G., LEWIS, D.R., NORRIS, J.D. & LAFFERTY, J.F. 2014 Mach 10 boundary-layer transition experiments on sharp and blunted cones. *AIAA Paper* 2014-3108.

MASLOV, A.A., SHIPLYUK, A.N., BOUNTIN, D.A. & SIDORENKO, A.A. 2006 Mach 6 boundary-layer stability experiments on sharp and blunted cones. *J. Spacecr. Rockets* **43** (1), 71–76.

PAREDES, P. 2014 Advances in global instability computations: from incompressible to hypersonic flow. PhD thesis, Technical University of Madrid.

PAREDES, P., CHOUDHARI, M.M. & LI, F. 2019*a* Laminar-turbulent transition upstream of the entropy-layer swallowing location in hypersonic boundary layers. *AIAA Paper* 2019-3215.

PAREDES, P., CHOUDHARI, M.M. & LI, F. 2020 Mechanism for frustum transition over blunt cones at hypersonic speeds. *J. Fluid Mech.* **894**, A22.

PAREDES, P., CHOUDHARI, M.M., LI, F., JEWELL, J.S. & KIMMEL, R.L. 2019*b* Nonmodal growth of traveling waves on blunt cones at hypersonic speeds. *AIAA J.* **57** (11), 4738–4749.

PAREDES, P., CHOUDHARI, M.M., LI, F., JEWELL, J.S., KIMMEL, R.L., MARINEAU, E.C. & GROSSIR, G. 2019*c* Nose-tip bluntness effects on transition at hypersonic speeds. *J. Spacecr. Rockets* **56** (2), 369–387.

PAREDES, P., HANIFI, A., THEOFILIS, V. & HENNINGSON, D. 2015 The nonlinear PSE-3D concept for transition prediction in flows with a single slowly-varying spatial direction. *Procedia IUTAM* **14**, 35–44.

PARZIALE, N.J. 2013 Slender-body hypervelocity boundary-layer instability. PhD thesis, California Institute of Technology.

ROTTA, N.R. 1966 Effects of nose bluntness on the boundary layer characteristics of conical bodies at hypersonic speeds. *Tech. Rep.* NYU-AA-66-66. New York University.

SETTLES, G.S. & FULGHUM, M.R. 2016 The focusing laser differential interferometer, an instrument for localized turbulence measurements in refractive flows. *Trans. ASME J. Fluid Engng* **138** (10), 101402.

STETSON, K.F. 1983 Nosetip bluntness effects on cone frustum boundary layer transition in hypersonic flow. *AIAA Paper* 1983-1763.

WAGNILD, R.M., CANDLER, G.V., LEYVA, I.A., JEWELL, J.S. & HORNUNG, H.G. 2010 Carbon dioxide injection for hypervelocity boundary layer stability. *AIAA Paper* 2010-1244.

WRIGHT, M.J., CANDLER, G.V. & BOSE, D. 1998 Data-parallel line relaxation method for the Navier–Stokes equations. *AIAA J.* **36** (9), 1603–1609.